Received: 19 November 2021 | Revised: 9 May 2022 | Accepted: 17 September 2022

DOI: 10.1002/cnm.3650

APPLIED RESEARCH

WILEY

# A PDE-regularized smoothing method for space–time data over manifolds with application to medical data

**Luca Ponti**[1] | **Simona Perotto**[2] | **Laura M. Sangalli**[2]

[1]Politecnico di Milano, Milan, Italy

[2]MOX-Department of Mathematics, Politecnico di Milano, Milan, Italy

**Correspondence**
Simona Perotto, MOX-Department of Mathematics, Politecnico di Milano, Piazza Leonardo da Vinci, 32, I-20133 Milan, Italy.
Email: simona.perotto@polimi.it

**Abstract**

We propose an innovative statistical-numerical method to model spatio-temporal data, observed over a generic two-dimensional Riemanian manifold. The proposed approach consists of a regression model completed with a regularizing term based on the heat equation. The model is discretized through a finite element scheme set on the manifold, and solved by resorting to a fixed point-based iterative algorithm. This choice leads to a procedure which is highly efficient when compared with a monolithic approach, and which allows us to deal with massive datasets. After a preliminary assessment on simulation study cases, we investigate the performance of the new estimation tool in practical contexts, by dealing with neuroimaging and hemodynamic data.

**KEYWORDS**

finite elements, fixed point algorithm, hemodynamics, neuroimaging, regularized regression

## 1 | INTRODUCTION

This work proposes a statistical-numerical methodology to analyze spatio-temporal data measured on general two-dimensional Riemanian manifold domains. These kinds of data are very common in diverse contexts, from Engineering to Applied Sciences. In an Engineering design process, for instance, it is standard to study time- as well as space-varying quantities of interest observed over the surface of a three-dimensional prototype in order to optimize the design pipeline (e.g., the aerodynamic forces exerted on the surface of an airfoil when dealing with the design of an airplane). In Environmental Science, it is of paramount importance to accurately model space–time data distributed over regions characterized by a complex orography, for example, in order to better understand the Earth processes, or to control pollution or global climate changes, or to optimize the exploitation of natural resources. In this paper, we focus on some applications which arise from Life Science. Figure 1 refers to one of the analyzed contexts. The panel on the left shows the mesh approximating the cortical surface of a brain, on which the hemodynamic signal induced by the neuronal activity on the cortical surface, shown in the right panel, has been observed at a certain time. Standard spatio-temporal techniques, that rely on the Euclidean distance, are not suited, in general, to handle data such as the ones in Figure 1. Due to folded geometry of the domain, such methods can yield highly inaccurate estimates, by incorrectly identifying as close, data locations that actually are far apart on the real geometry. Thus, values observed over two distinct gyri could be artificially linked each other, although, in practice, separated by a sulcus. As a consequence, in order to obtain accurate estimates on complex manifolds, it becomes mandatory to appropriately comply with the complex geometry of the domain.

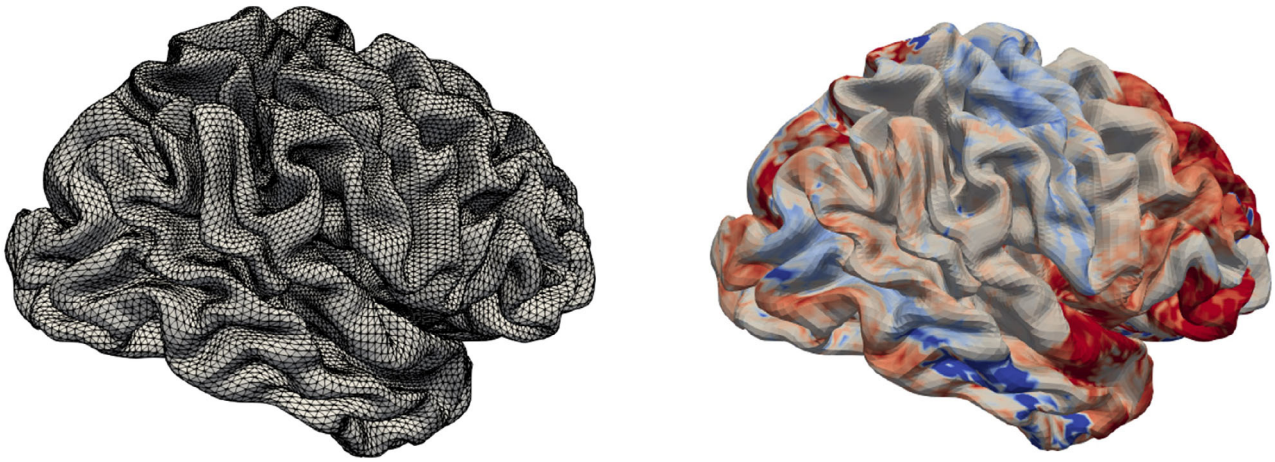

**FIGURE 1** Neuroimaging signal on a cerebral cortex: triangular mesh modeling the cortical surface (left); fMRI signal associated with neuronal activity distributed over the cortex at a certain temporal instant (right)

The diversified demands characterizing a so large number of different application fields justify the strong interest for data analysis over two-dimensional Riemannian manifolds, both in the statistical and in the numerical literature. Nevertheless, the available methodologies are so far confined to special manifolds, such as spheres or sphere-like domains (see, e.g.,[1–7] and the references therein), or to the spatial dimension only (see, e.g.,[8–15]). The challenge tackled in this paper is consequently twofold, since dealing with space–time data over a general two-dimensional manifold. To this aim, we propose a computational procedure which belongs to, and further strongly advances, the class of Spatial Regression with PDE regularization methods reviewed in Reference [16]. In particular, we adopt an estimation functional which combines a least-square data-fidelity criterion with a regularizing term based on the heat equation. The work is inspired by the regression model for spatial data over manifold domains considered in Reference [12], as well as to the spatio-temporal model for planar domains proposed in Reference [17]. In more detail, here we discretize the problem directly on the manifold instead of resorting to a conformal flattening of the domain as in Reference [12]. This allows us to avoid the approximation error characterizing the flattening step. Moreover, we use an iterative fixed point scheme to solve the discrete problem instead of the monolithic approach adopted in Reference [17]. Such a choice ensures a highly computational efficiency, and makes it possible to handle massive datasets, such as those characterizing the applied problems mentioned above.

The paper is organized as follows: Section 2 provides some notation related to the differential operators on Riemannian manifolds and to the associated function spaces. Section 3 introduces the proposed PDE-regularized spatio-temporal smoothing method. Section 4 details the discretization used to solve the estimation problem, by distinguishing between the monolithic approach and the new fixed point-based algorithm. Section 5 shows the good performances of the new method through simulation study cases, whereas Section 6 focuses on two applications in Life Science, by considering neuroimaging data and the study of cerebral aneurysms. Finally, Section 7 outlines possible directions for a future research.

## 2 | PRELIMINARIES AND NOTATION

We denote by $\mathcal{M} \subset \mathbb{R}^3$ the two-dimensional Riemannian manifold that constitues the spatial domain of interest, and by $[0, T] \subset \mathbb{R}$ the considered time window.

We associate with manifold $\mathcal{M}$ the Laplace-Beltrami operator, $\Delta_{\mathcal{M}}$, and the gradient, $\nabla_{\mathcal{M}}$, involved in the definition of the estimation problem and of the corresponding approximation, respectively. In particular, the Laplace-Beltrami operator generalizes the standard Laplacian to the case of a function defined over a manifold, by providing a simple measure of the local curvature of such a function. Moreover, operator $\Delta_{\mathcal{M}}$ is invariant with respect to Euclidean transformations (rotations, translations and reflections) of the spatial coordinates.

Concerning the function spaces, we introduce the space $C^0(\mathcal{M})$ of the functions continuous on $\mathcal{M}$ (which is meant associated with the closure of $\mathcal{M}$ when $\mathcal{M}$ is an open manifold), and the Sobolev space, $H^k(\mathcal{M})$, of the functions $u : \mathcal{M} \to \mathbb{R}$ which belong to $L^2(\mathcal{M})$ (i.e., which are square-integrable on $\mathcal{M}$), together with the associated partial derivatives up to the order $k$.[18] Note that $L^2(\mathcal{M})$ coincides with $H^0(\mathcal{M})$.

Finally, as space–time function setting, we consider the space $L^2\big(0, T; H^k(\mathcal{M})\big)$ of the functions $u$ defined over $(0, T)$ and taking values in $H^k(\mathcal{M})$, such that $\int_0^T \|u(t)\|^2_{H^k(\mathcal{M})} dt < +\infty$.[18]

## 3 | REGRESSION ANALYSIS WITH PDE REGULARIZATION

We consider $n$ data locations, $\{\mathbf{p}_i, i = 1, ..., n\}$, on manifold $\mathcal{M}$, and $m$ temporal instants, $t_1, t_2, ..., t_m$, in the time interval $[0, T]$, with $0 = t_1 < t_2 < ... < t_m = T$. We denote by $z_{ij}$ the value of a real-valued random variable of interest, when observed at the space–time location $(\mathbf{p}_i, t_j)$, for $i = 1, ..., n$ and $j = 1, ..., m$. We assume that the random variable coincides with a noisy observation of a smooth function, $f : \mathcal{M} \times [0, T] \to \mathbb{R}$, according to the model

$$z_{ij} = f(\mathbf{p}_i, t_j) + \epsilon_{ij} \quad \text{for } i = 1, ..., n,\ j = 1, ..., m, \tag{1}$$

where $\epsilon_{ij}$ are independent measurement errors characterized by a zero mean and a finite variance. Additionally, we assume that $f$ is twice continuously differentiable in space and continuously differentiable in time.

Our goal is to estimate the space–time field $f$ in (1) in the presence of an a priori knowledge on the phenomenon of interest. In particular, as in Reference [17], we assume that the problem under study can be described in terms of a time-dependent law, represented by a parabolic Partial Differential Equation (PDE). The problem-specific information may include also the Boundary Conditions (B.C.) when $\mathcal{M}$ is an open manifold, and the Initial Condition (I.C.), that model the behavior of the field $f$ at the boundary, $\partial\Omega \times \{0, T\}$, of the space–time domain of interest.

We propose to estimate $f$ by minimizing the regularized sum of squared function errors

$$J_\lambda(\phi) = \sum_{i=1,...,n} \sum_{j=1,...,m} \big[z_{ij} - \phi(\mathbf{p}_i, t_j)\big]^2 + \lambda \int_0^T \int_{\mathcal{M}} \left(\Delta_{\mathcal{M}}\phi - \frac{\partial \phi}{\partial t}\right)^2 d\mathbf{p}dt, \tag{2}$$

with $\phi : \mathcal{M} \times [0, T] \to \mathbb{R}$ twice continuously differentiable in space and continuously differentiable in time, $(\mathbf{p}, t)$ the generic space–time coordinate varying in $\mathcal{M} \times [0, T]$, and where $\lambda$ is a positive smoothing parameter.

Functional $J_\lambda$ formalizes a trade-off between a data fitting and a model fidelity criterion. On the one hand, the sum of the squared function errors pushes the solution to the minimization problem, denoted by $\widehat{f}$, close to the observed data $z_{ij}$ when evaluated at the space–time locations $(\mathbf{p}_i, t_j)$. On the other hand, the penalizing term controls the regularity, in space and time, of $\widehat{f}$. In particular, the employment of the Laplace-Beltrami operator ensures that the smoothness of $\widehat{f}$ does not depend on the orientation of the domain or of the coordinate system we adopt. Finally, parameter $\lambda$ tunes the trade-off between data fidelity and regularity, so that the higher the parameter $\lambda$, the more regular the estimate; vice versa, the lower the parameter $\lambda$, the closer the fit to the observed data.

It can be checked that the estimation problem

$$\text{find } \widehat{f} \text{ such that } \widehat{f} = \arg\min_{\phi} J_\lambda(\phi) \tag{3}$$

is well-defined in the space $V^2_T(\mathcal{M})$, with

$$V^s_T(\mathcal{M}) = \left\{ v \in L^2\big(0, T; H^s(\mathcal{M}) \cap C^0(\mathcal{M})\big) : \frac{\partial v}{\partial t} \in L^2\big(0, T; L^2(\mathcal{M})\big) + \text{B.C. and I.C.} \right\} \tag{4}$$

for $s \in \mathbb{N}^+$, and where proper boundary and initial conditions have to be included according to the specific problem at hand.

In this paper, we focus on the proposal of an efficient numerical approximation for the estimation problem (3). It turns out that the estimator $\widehat{f}$ minimizing the cost functional $J_\lambda$ in $V^2_T(\mathcal{M})$ satisfies the identity

$$\sum_{i=1,\dots,n}\sum_{j=1,\dots,m}\widehat{f}(\mathbf{p}_i,t_j)q(\mathbf{p}_i,t_j)+\lambda\int_0^T\int_{\mathcal{M}}\left(\Delta_{\mathcal{M}}\widehat{f}-\frac{\partial\widehat{f}}{\partial t}\right)\left(\Delta_{\mathcal{M}}q-\frac{\partial q}{\partial t}\right)d\mathbf{p}dt = \sum_{i=1,\dots,n}\sum_{j=1,\dots,m}q(\mathbf{p}_i,t_j)z_{ij} \tag{5}$$

for any function $q\in V_T^2(\mathcal{M})$. Equation (5) can be rewritten as a system of coupled parabolic problems, by introducing a suitable auxiliary function $g$ defined on $\mathcal{M}$.[12] Thus, we look for the pair $\left(\widehat{f},g\right)\in V_T^1(\mathcal{M})\times V_T^1(\mathcal{M})$, with $V_T^1(\mathcal{M})$ defined according to (4), such that,

$$\begin{cases}\displaystyle\int_0^T\int_{\mathcal{M}}\nu g\,d\mathbf{p}dt+\int_0^T\int_{\mathcal{M}}\left(\nabla_{\mathcal{M}}\widehat{f}\cdot\nabla_{\mathcal{M}}\nu+\frac{\partial\widehat{f}}{\partial t}\nu\right)d\mathbf{p}dt=0\\ \displaystyle\sum_{i=1,\dots,n}\sum_{j=1,\dots,m}\widehat{f}(\mathbf{p}_i,t_j)q(\mathbf{p}_i,t_j)-\lambda\int_0^T\int_{\mathcal{M}}\left(\nabla_{\mathcal{M}}g\cdot\nabla_{\mathcal{M}}q-\frac{\partial g}{\partial t}q\right)d\mathbf{p}dt\\ \displaystyle=\sum_{i=1,\dots,n}\sum_{j=1,\dots,m}q(\mathbf{p}_i,t_j)z_{ij},\end{cases} \tag{6}$$

with $(\nu,q)\in V_T^1(\mathcal{M})\times V_T^1(\mathcal{M})$. We remark that the first problem in (6) coincides with a standard (forward) parabolic PDE, whereas the problem associated with $g$ constitutes a backward parabolic PDE, since the time derivative and the diffusive term are characterized by an opposite sign. As a consequence, the initial condition $\widehat{f}(\mathbf{p},0)=\widetilde{f}_0$ is added to the first equation, while the ending condition $g(\mathbf{p},T)=\widetilde{g}_T$ completes the second PDE.

Concerning the conditions to be assigned on $\partial\Omega$, we will select the boundary data according to the test case at hand. In particular, the essential boundary conditions will be explicitly included in the definition of space $V_T^1(\mathcal{M})$.

Formulation (6) turns out to be instrumental in view of the discrete counterpart of problem (3). In particular, the numerical procedure proposed in Section 4.2 will be characterized by a considerable computational efficiency, thanks to the introduction of an ad-hoc iterative algorithm. This feature will allow us to handle massive datasets, typical of several applicative contexts.

## 4 | DISCRETIZATION OF THE ESTIMATION PROBLEM

This section represents the methodological core of the paper. We provide an improvement in terms of computational efficiency of the approach used in Reference [17] to tackle system (6) in the simplified case of data distributed over a planar domain according to specific sampling designs (e.g., pointwise spatial/interval temporal data, areal spatial/pointwise temporal data, areal spatial/interval temporal data). The final goal is to finalize a handy and accurate procedure able to efficiently analyze considerable amount of space–time data, observed over general two-dimensional Riemannian manifold domains.

In particular, to approximate the system of parabolic PDEs in (6), we have to define a discretization both in space and time. To discretize the space, we introduce a conformal triangulation, $\mathcal{T}_h=\{K\}$, of the manifold $\mathcal{M}$, $h$ being the characteristic mesh size. To discretize the time dependence, we consider a partition, $\tau_1=0<\tau_2<\cdots<\tau_M=T$, of the time window $(0,T]$ into $(M-1)$ subintervals, $(\tau_{k-1},\tau_k]$, of length $\Delta t$, with $k=2,\dots,M$. For simplicity of exposition, we assume that the vertices of $\mathcal{T}_h$ exactly coincide with the data locations $\mathbf{p}_i$, and that the times when data are collected identify the time partition, so that $M\equiv m$ and $\tau_j\equiv t_j$ for $j=1,\dots,m$. The reader interested to the more general case where mesh vertices do not necessarily coincide with the data locations is referred, e.g., to References [17,19].

Then, we define the finite element space, $V_h^r(\mathcal{M})=\left\{v_h\in C^0(\mathcal{M}):v_h\big|_K\in\mathbb{P}^r(K),\forall K\in\mathcal{T}_h\right\}$, associated with the tessellation $\mathcal{T}_h$, where $\mathbb{P}^r(K)$ denotes the space of the polynomials of degree $r$ defined on $K$. Notice that the (essential) boundary conditions characterizing space $V_T^1(\mathcal{M})$ in (6) are inherited by the discrete space $V_h^r(\mathcal{M})$.

We consider a Lagrangian basis $\mathscr{B}=\left\{\psi_1,\dots,\psi_{N_T}\right\}$ of the space $V_h^r(\mathcal{M})$, associated with the nodes $\boldsymbol{\xi}_1,\dots,\boldsymbol{\xi}_{N_T}$ of the triangulation, being $\dim\left(V_h^r(\mathcal{M})\right)=N_T$ (we remind that the nodes are, in general, a super-set of the mesh vertices; only

for linear finite elements [$r = 1$], the nodes exactly coincide with the vertices of $\mathcal{T}_h$). Thus, each function $v_h \in V_h^r(\mathcal{M})$ can be expressed in terms of this basis as $v_h(\mathbf{x}) = \sum_{i=1}^{N_\mathcal{T}} v_h(\boldsymbol{\xi}_i)\psi_i(\mathbf{x}) = \mathbf{v}^T\boldsymbol{\psi}(\mathbf{x})$, where vector $\boldsymbol{\psi}(\mathbf{x}) = \left[\psi_1(\mathbf{x}), ..., \psi_{N_\mathcal{T}}(\mathbf{x})\right]^T$ collects the $N_\mathcal{T}$ finite element basis functions at the generic point $\mathbf{x} \in \mathcal{M}$, while vector $\mathbf{v} = \left[v_h(\boldsymbol{\xi}_1), ..., v_h\left(\boldsymbol{\xi}_{N_\mathcal{T}}\right)\right]^T \in \mathbb{R}^{N_\mathcal{T}}$ gathers the evaluation of function $v_h$ at the $N_\mathcal{T}$ nodes.

In addition, if we define the vector $\mathbf{v}_n = [v_h(\mathbf{p}_1), ..., v_h(\mathbf{p}_n)]^T \in \mathbb{R}^n$ of the evaluations of function $v_h$ at the $n$ data locations, $\mathbf{p}_1$, ...$\mathbf{p}_n$, and the matrix $\Psi = (\boldsymbol{\psi}^T(\mathbf{p}_1), ..., \boldsymbol{\psi}^T(\mathbf{p}_n)) \in \mathbb{R}^{n \times N_\mathcal{T}}$ of the evaluations of the basis functions at the same points, we can relate vectors $\mathbf{v}$ and $\mathbf{v}_n$ via the equality $\mathbf{v}_n = \Psi\mathbf{v}$. In particular, for $r = 1$, matrix $\Psi$ reduces to the identity matrix, $I \in \mathbb{R}^{n \times n}$, and $\mathbf{v} \equiv \mathbf{v}_n$.

By extending the notation above, we denote by

$$\mathbf{v}^k = \left[v_h(\boldsymbol{\xi}_1, t_k), ..., v_h\left(\boldsymbol{\xi}_{N_\mathcal{T}}, t_k\right)\right]^T \in \mathbb{R}^{N_\mathcal{T}}, \qquad \mathbf{v}_n^k = [v_h(\mathbf{p}_1, t_k), ..., v_h(\mathbf{p}_n, t_k)]^T \in \mathbb{R}^n \tag{7}$$

the vectors gathering the values taken at time $t_k$ by $v_h$ at the finite element nodes and at the data locations, respectively, so that $\mathbf{v}_n^k = \Psi\mathbf{v}^k$, where, for $r = 1$ it holds $\mathbf{v}^k \equiv \mathbf{v}_n^k$ with $k = 1, ..., m$, being $\boldsymbol{\xi}_i \equiv \mathbf{p}_i$.

In the next sections, we introduce two different approximations based on the above space–time discretization. The former has been recently proposed in the literature in the simpler case of space–time data observed over planar domains[17] and represents the reference context for the numerical assessment of this paper (see Section 4.1); the latter coincides with the new proposed approach which aims at being computationally highly more effective (see Section 4.2).

## 4.1 | A monolithic approach

We provide here the space–time discretization scheme proposed in Reference [17]. The authors employ finite elements of degree $r$ to approximate the space, combined with the $\theta$-method for the time discretization. This leads to discretize time derivatives through an incremental ratio, whereas the other time-dependent terms are replaced by a convex linear combination of their values at times $t_k$ and $t_{k+1}$.[20] In particular, in Reference [17], the authors resort to the backward Euler scheme ($\theta = 1$), so that, for each $k = 1, ..., m - 1$, the following system is solved for $\widehat{f}_h^{k+1}$ and $g_h^k$, both in $V_h^r(\mathcal{M})$:

$$\begin{cases} \displaystyle\int_\mathcal{M} \rho_h g_h^k \, d\mathbf{p} + \int_\mathcal{M} \nabla_\mathcal{M} \widehat{f}_h^{k+1} \cdot \nabla_\mathcal{M} \rho_h \, d\mathbf{p} + \int_\mathcal{M} \frac{\widehat{f}_h^{k+1} - \widehat{f}_h^k}{\Delta t} \rho_h \, d\mathbf{p} = 0 \\ \boldsymbol{\varphi}_n^T \widehat{\mathbf{f}}_n^{k+1} + \lambda \displaystyle\int_\mathcal{M} \frac{g_h^{k+1} - g_h^k}{\Delta t} \varphi_h \, d\mathbf{p} - \lambda \int_\mathcal{M} \nabla_\mathcal{M} g_h^k \cdot \nabla_\mathcal{M} \varphi_h \, d\mathbf{p} = \boldsymbol{\varphi}_n^T \mathbf{z}_n^{k+1} \\ \widehat{f}_h^1 = \widetilde{f}_{h,1}, \quad g_h^m = \widetilde{g}_{h,m}, \end{cases} \tag{8}$$

with $\rho_h$, $\varphi_h \in V_h^r(\mathcal{M})$, where $\widehat{f}_h^j = \widehat{f}_h(\mathbf{p}, t_j)$, $g_h^j = g_h(\mathbf{p}, t_j) \in V_h^r(\mathcal{M})$ denote the finite element approximation for function $\widehat{f}$ and g, respectively at time $t_j$, with $j = 1, ..., m$, $\widetilde{f}_{h,1}$ and $\widetilde{g}_{h,m}$ are suitable approximations in $V_h^r(\mathcal{M})$ of the initial data $\widetilde{f}_1$ and of the ending data $\widetilde{g}_m$, and where we have introduced the vectors $\widehat{\mathbf{f}}_n^{k+1} = \left[\widehat{f}_h(\mathbf{p}_1, t_{k+1}), ..., \widehat{f}_h(\mathbf{p}_n, t_{k+1})\right]^T$, $\mathbf{z}_n^{k+1} = [z_{1k+1}, ..., z_{nk+1}]^T$, $\boldsymbol{\varphi}_n = [\varphi_h(\mathbf{p}_1), ..., \varphi_h(\mathbf{p}_n)]^T \in \mathbb{R}^n$. Notice that, according to this space–time approximation, the test functions are only space-dependent, in contrast to formulation (6) (and to the discretization adopted in the next section).

Following,[12,17] in order to provide the algebraic counterpart of system (8), we introduce the matrices of dimensionality $N_\mathcal{T}$

$$R_0 = \int_\mathcal{M} \boldsymbol{\psi}\boldsymbol{\psi}^T \, d\mathbf{p}, \qquad R_1 = \int_\mathcal{M} \nabla_\mathcal{M}\boldsymbol{\psi}^T \, (\nabla_\mathcal{M}\boldsymbol{\psi})^T \, d\mathbf{p},$$

where $(\nabla_\mathcal{M}\boldsymbol{\psi})^T$ is the transpose of the array $\nabla_\mathcal{M}\boldsymbol{\psi}(\mathbf{p}) = \left[\nabla\psi_1(\mathbf{p}), ..., \nabla\psi_{N_\mathcal{T}}(\mathbf{p})\right]^T$ collecting the gradient of the $N_\mathcal{T}$ finite element basis functions at the generic point $\mathbf{p} \in \mathcal{M}$, whereas $\nabla_\mathcal{M}\boldsymbol{\psi}^T = \nabla_\mathcal{M}\boldsymbol{\psi}^T(\mathbf{p}) = \left[(\nabla\psi_1)^T(\mathbf{p}), ..., \left(\nabla\psi_{N_\mathcal{T}}\right)^T(\mathbf{p})\right]^T$. It follows that, for any $u_h$, $w_h \in V_h^r(\mathcal{M})$,

$$\int_{\mathcal{M}} u_h w_h \, d\mathbf{p} = \mathbf{u}^T R_0 \mathbf{w}, \qquad \int_{\mathcal{M}} \nabla_{\mathcal{M}} u_h \cdot \nabla_{\mathcal{M}} w_h \, d\mathbf{p} = \mathbf{u}^T R_1 \mathbf{w},$$

vectors $\mathbf{u} = \left[u_h(\boldsymbol{\xi}_1), ..., u_h\left(\boldsymbol{\xi}_{N_\mathcal{T}}\right)\right]^T$, $\mathbf{w} = \left[w_h(\boldsymbol{\xi}_1), ..., w_h\left(\boldsymbol{\xi}_{N_\mathcal{T}}\right)\right]^T \in \mathbb{R}^{N_\mathcal{T}}$ gathering the values taken by functions $u_h$ and $w_h$ at the mesh nodes.

From now on, we take $r = 1$, so that $N_\mathcal{T} = n$. Thus, the algebraic counterpart of the space–time discretization in (8) turns out to be

$$\begin{cases} R_0 \mathbf{g}_n^k + R_1 \widehat{\mathbf{f}}_n^{k+1} + R_0 \dfrac{\widehat{\mathbf{f}}_n^{k+1} - \widehat{\mathbf{f}}_n^k}{\Delta t} = 0 \\ \Psi^T \Psi \widehat{\mathbf{f}}_n^{k+1} + \lambda R_0 \dfrac{\mathbf{g}_n^{k+1} - \mathbf{g}_n^k}{\Delta t} - \lambda R_1 \mathbf{g}_n^k = \Psi^T \mathbf{z}_n^{k+1}, \end{cases} \tag{9}$$

with $k = 1, ..., m-1$, $\widehat{\mathbf{f}}_n^1 = \left[\widetilde{f}_{h,1}(\mathbf{p}_1), ..., \widetilde{f}_{h,1}(\mathbf{p}_n)\right]^T$, $\mathbf{g}_n^m = \left[\widetilde{g}_{h,m}(\mathbf{p}_1), ..., \widetilde{g}_{h,m}(\mathbf{p}_n)\right]^T \in \mathbb{R}^n$, and where, in accordance with the notation in (7), $\widehat{\mathbf{f}}_n^k = \left[\widehat{f}_h(\mathbf{p}_1, t_k), ..., \widehat{f}_h(\mathbf{p}_n, t_k)\right]^T$, $\mathbf{g}_n^j = \left[g_h\left(\mathbf{p}_1, t_j\right), ..., g_h\left(\mathbf{p}_n, t_j\right)\right]^T \in \mathbb{R}^n$ for $j = k, k+1$.

System (9) is sparse since the Lagrangian basis $\mathcal{B}$ is locally supported. Nevertheless, the system is fully coupled due to the opposite time direction characterizing the equations for $\widehat{f}_h$ and $g_h$. Such a coupling leads to adopt a monolithic approach[17] when solving (9). This means to consider simultaneously all the spatial data locations and all the involved times, namely to solve a *unique* system with a dimensionality equal to $2mn$ (see Figure 2). This feature might represent an issue from a computational viewpoint, in particular when dealing with large datasets (i.e., for large values of $m$ and $n$). As a consequence, complex geometries or long time-series are ruled out by the monolithic method, which, in such contexts, becomes very time- and memory-consuming. This is the case of the applications tackled in Section 6 which are out of reach for the monolithic approach when codes are run on a standard laptop* .

All these considerations justify the proposal in the next section of a new procedure, which offers us an alternative to the monolithic approach.

## 4.2 | A new fixed point-based algorithm

The procedure here proposed aims at commuting the whole system (9) into smaller problems in order to make affordable the management of complex amounts of data.

In particular, to tackle the coupling between the two equations in (9), we resort to a fixed point approach.[20] Additionally, we adopt a space–time discretization alternative to the one characterizing the monolithic approach. In particular, to be compliant with the weak formulation in (6), where the trial and the test functions depend both on the space and time, we employ space–time finite elements, continuous in space and time.[21,22] Thus, in the generic time interval,

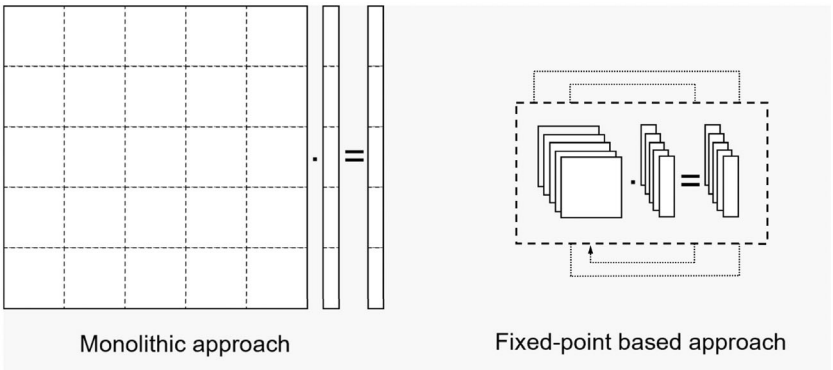


FIGURE 2 Sketch of the dimensionality characterizing the algebraic system associated with the monolithic (left) and with the fixed point-based (right) algorithm

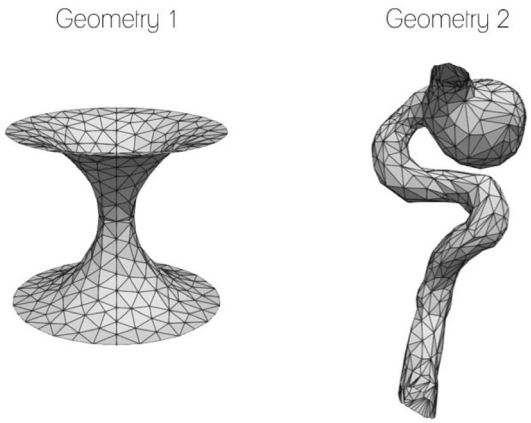


**FIGURE 3** Geometries for the simulation studies. Geometry 1: a benchmark geometry. Geometry 2: simplification of a patient-specific inner carotid artery affected by an aneurysm

$(\tau_{k-1}, \tau_k]$, a fully discrete function, $w_h$, can be expanded as $\sum_{j=0}^{s} t^j w_{h,j}(\mathbf{p})$, that is, as a linear combination of functions, $w_{h,j}$, belonging to the finite element space, $V_h^r(\mathcal{M})$, with coefficients coinciding with suitable powers of the time independent variable, $t$. Throughout the paper, we make the choice $r = 1$, $s = 0$ in view of a fair comparison between the monolithic and the new approach.

We replace the algebraic system (9) with the new one

$$\begin{cases} R_0 \mathbf{g}_n^{k+1} + R_1 \widehat{\mathbf{f}}_n^{k+1} + R_0 \dfrac{\widehat{\mathbf{f}}_n^{k+1} - \widehat{\mathbf{f}}_n^{k}}{\Delta t} = 0 \\ \Psi^T \Psi \widehat{\mathbf{f}}_n^{k} + \lambda R_0 \dfrac{\mathbf{g}_n^{k+1} - \mathbf{g}_n^{k}}{\Delta t} - \lambda R_1 \mathbf{g}_n^{k} = \Psi^T \mathbf{z}_n^{k}, \end{cases} \tag{10}$$

with $k = 1, ..., m-1$, where the same notations as in (9) are here adopted. Analogously to a semi-implicit scheme, all the time-dependent terms in the equation associated with $\widehat{f}$ are evaluated at time $t^{k+1}$, whereas the time-dependent contributions in the equation to be solved for $g$ are considered at time $t^k$.

Now, for each $k = 1, ..., m$, we yield a sequence of approximations $\left\{ \left( \widehat{\mathbf{f}}_n^{k,j}, \mathbf{g}_n^{k,j} \right) \right\}$ for the solution $\left( \widehat{\mathbf{f}}_n^{k}, \mathbf{g}_n^{k} \right)$ of system (10) via an iterative fixed point algorithm, $j$ being the fixed point iteration index. Then, a check on the accuracy, combined with a maximum number of iterations, is used to stop the iterative procedure.

To start the algorithm, we have to select the initial guess. In particular:

1. we compute the values $\widehat{\mathbf{f}}_n^{k,0}$, for $k = 2, ..., m$, by referring to the steady case (see Proposition 2 in Reference [12]), that is, by solving the $(m-1)$ problems

$$\left( \Psi^T \Psi + \lambda R_1 R_0^{-1} R_1 \right) \widehat{\mathbf{f}}_n^{k,0} = \Psi^T \mathbf{z}_n^{k}; \tag{11}$$

2. we compute the values $\mathbf{g}_n^{k,0}$, for $k = m-1, ..., 1$, by solving the $(m-1)$ problems

$$\Psi^T \Psi \widehat{\mathbf{f}}_n^{k,0} + \lambda R_0 \frac{\mathbf{g}_n^{k+1,0} - \mathbf{g}_n^{k,0}}{\Delta t} - \lambda R_1 \mathbf{g}_n^{k,0} = \Psi^T \mathbf{z}_n^{k} \tag{12}$$

by using the values obtained in (11) for the vectors $\widehat{\mathbf{f}}_n^{k,0}$, for $k = 2, ..., m$, and by setting, for simplicity, $\mathbf{g}_n^{m,0} = \mathbf{0}$ and $\widehat{\mathbf{f}}_n^{1,0} = \widehat{\mathbf{f}}_n^{1}$.

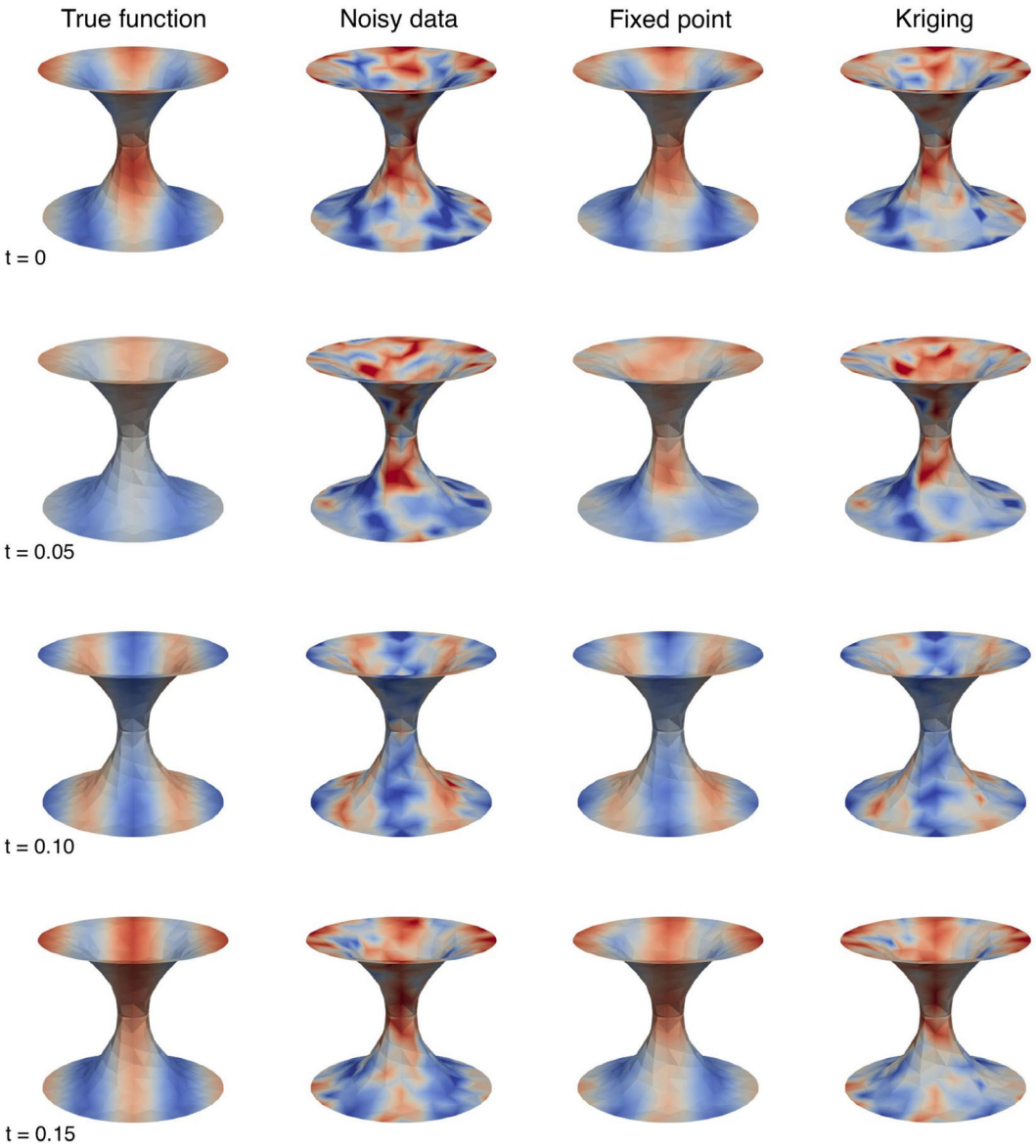


**FIGURE 4** Geometry 1: true function $f$ (first column) generated in the first simulation repetition, at time $t = 0$[s] (first row), 0.05 [s] (second row), 0.10[s] (third row) and 0.15[s] (last row); noisy data (second column); estimate provided by the proposed fixed point-based algorithm (third column) and by the spatio-temporal kriging (fourth column)

Then, at the generic iteration, $j$ (with $j \geq 1$), of the fixed point scheme, we update the pair $\left(\widehat{\mathbf{f}}_n^{k,j-1}, \mathbf{g}_n^{k,j-1}\right)$, for $k = 1$, ..., $m$, by computing the new pair $\left(\widehat{\mathbf{f}}_n^{k,j}, \mathbf{g}_n^{k,j}\right)$, such that:

i. for $k = 1$,

$$\begin{cases} \widehat{\mathbf{f}}_n^{1,j} = \widehat{\mathbf{f}}_n^{1} \\ \lambda\left(R_1 + \dfrac{1}{\Delta t} R_0\right)\mathbf{g}_n^{1,j} = \dfrac{\lambda}{\Delta t} R_0 \mathbf{g}_n^{2,j-1} + \Psi^T\left(\Psi\widehat{\mathbf{f}}_n^{1} - \mathbf{z}_n^{1}\right); \end{cases}$$

ii. for $k = 2$, ..., $m - 1$,

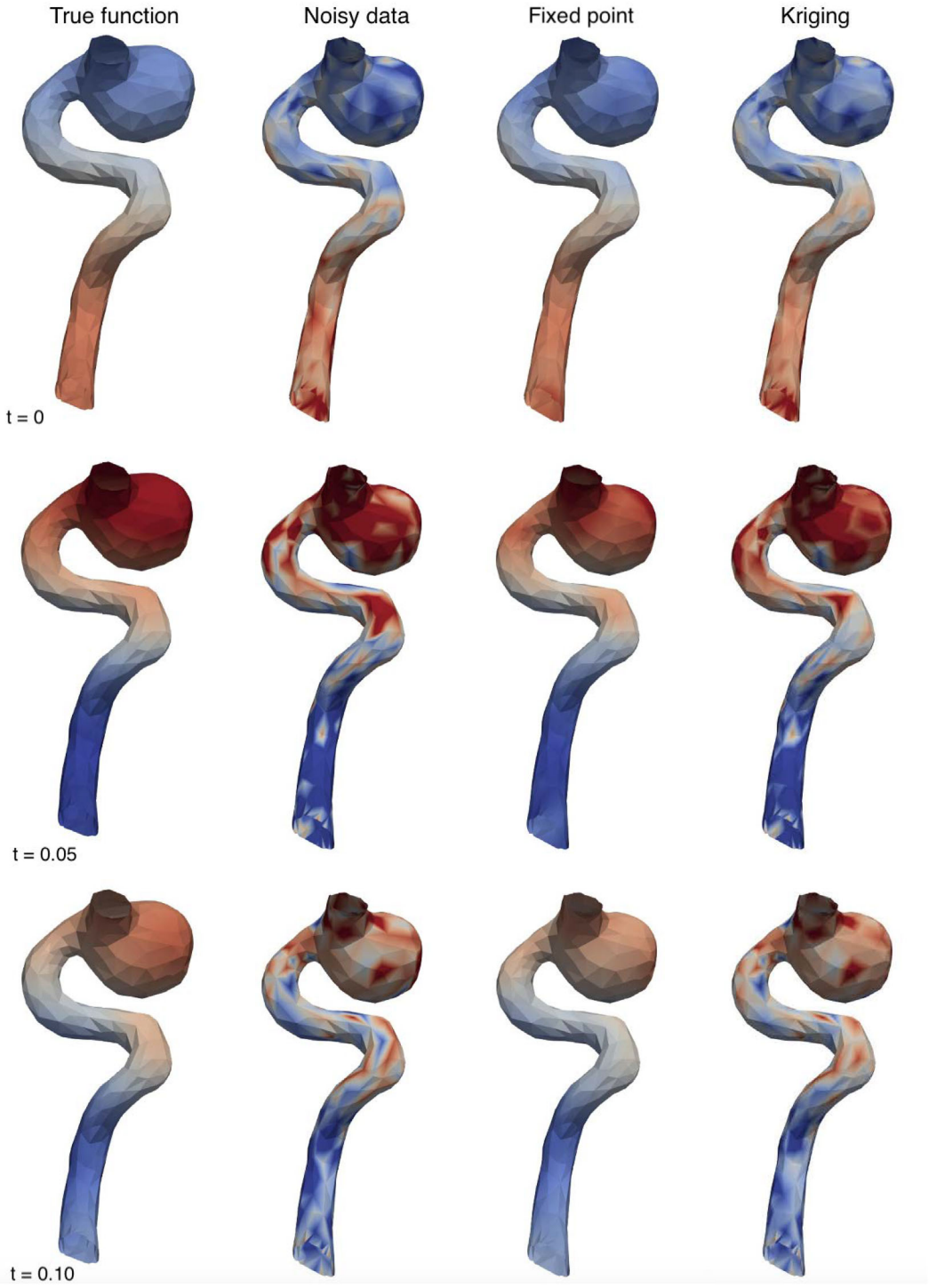


**FIGURE 5** Geometry 2: true function $f$ (first column) generated in the first simulation repetition, at time $t = 0$[s] (first row), 0.05 [s] (second row), 0.10[s] (third row); noisy data (second column); estimate provided by the proposed fixed point-based algorithm (third column) and by the spatio-temporal kriging (fourth colum)

$$\begin{bmatrix} R_1 + \frac{1}{\Delta t} R_0 & R_0 \\ \Psi^T \Psi & -\lambda \left( R_1 + \frac{1}{\Delta t} R_0 \right) \end{bmatrix} \begin{bmatrix} \widehat{\mathbf{f}}_n^{k,j} \\ \mathbf{g}_n^{k,j} \end{bmatrix} = \begin{bmatrix} \frac{1}{\Delta t} R_0 \widehat{\mathbf{f}}_n^{k-1,j-1} \\ \Psi^T \mathbf{z}_n^k - \frac{\lambda}{\Delta t} R_0 \mathbf{g}_n^{k+1,j-1} \end{bmatrix}; \tag{13}$$

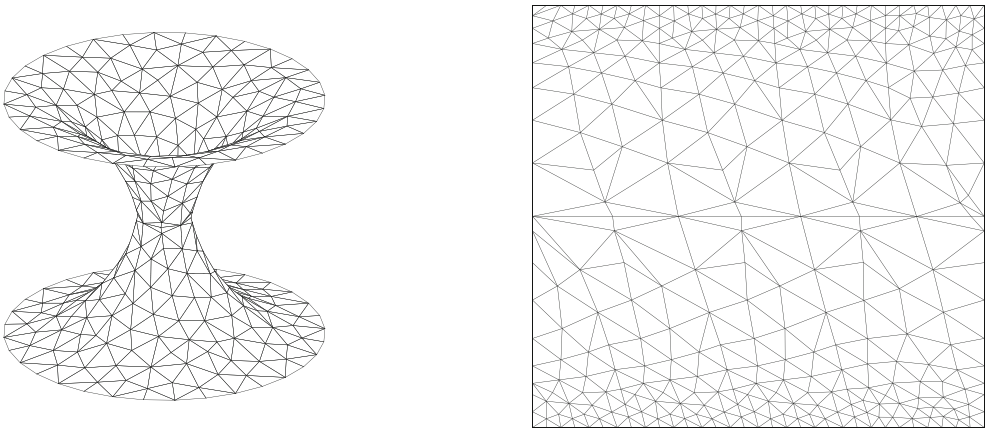

FIGURE 6 Geometry 1: original geometry (left); conformal flattening of the geometry used for the implementation of kriging (right)

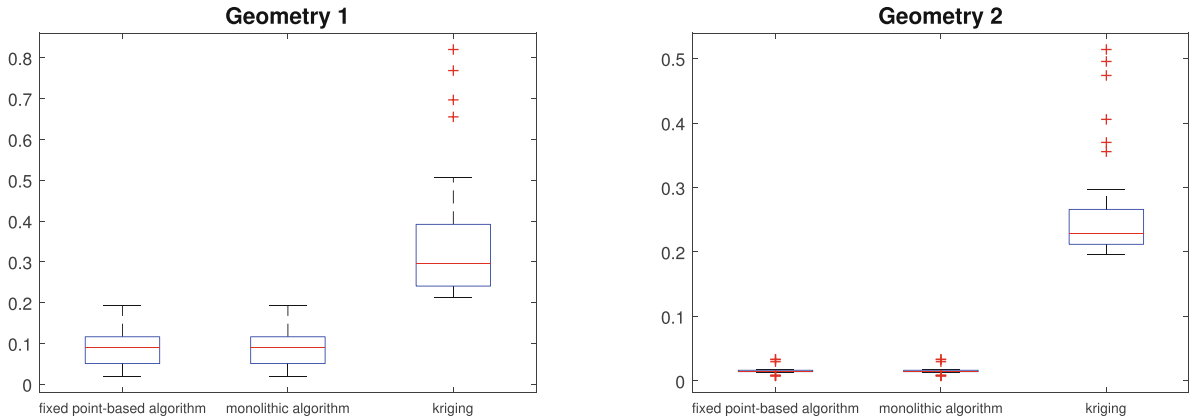


FIGURE 7 Geometries 1 and 2: box plots for the Mean Square Error (MSE) associated with the estimates provided by the fixed point-based method, by the monolithic approach and by kriging, over the 50 simulation repetitions with test functions generated as in (14).

iii. for $k = m$,

$$\begin{cases} \left(R_1 + \frac{1}{\Delta t} R_0\right) \widehat{\mathbf{f}}_n^{m,j} = \left(\frac{1}{\Delta t} R_0 \widehat{\mathbf{f}}_n^{m-1,j-1} - R_0 \mathbf{g}_n^{m,j-1}\right) \\ \mathbf{g}_n^{m,j} = \mathbf{0}. \end{cases}$$

The decoupling effect introduced by the fixed point iterations allows us to carry out all the computations in i–iii simultaneously, in the spirit of a Jacobi solver. We highlight that, although the evident similarity between systems (9) and (13), with the new algorithm we are solving, at the same time, $m$ systems of dimension $2n$ instead of a unique system of dimension $2mn$ as for the monolithic approach (see Figure 2). This difference in terms of dimensionality justifies the considerable computational gain characterizing the fixed point-based approach when compared with the monolithic formulation, as verified in Section 6 (see Figure 8).

Finally, the fixed point algorithm is stopped by introducing a tolerance, `TOL`, on the relative variation of the cost functional $J_\lambda$ in (2), when evaluated on two consecutive approximations, and after setting a maximum number, `NMax`, of iterations.

The two next sections are meant to numerically investigate the reliability and the efficiency of the fixed point-based algorithm, first when applied to simulation case studies and then by considering a real datasets.

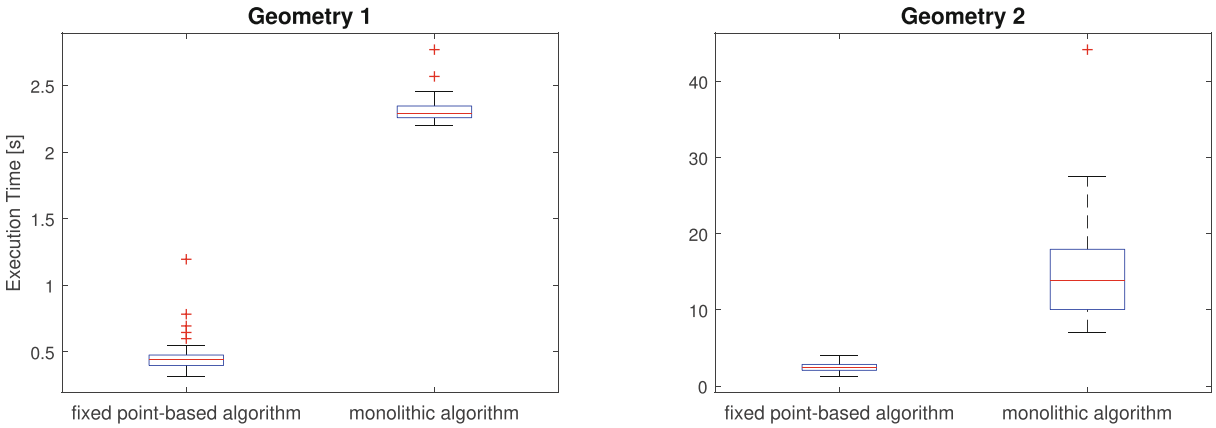


**FIGURE 8** Geometries 1 and 2: box plots for the execution time ([s]) associated with the estimates provided by the fixed point-based and by the monolithic approach over the 50 simulation repetitions with test functions generated as in (14)

## 5 | SIMULATION STUDIES

In this section, we assess the performances of the new algorithm introduced in Section 4.2 when applied to spatio-temporal data. We compare the proposed method with kriging, the most commonly used technique to analyze spatial and spatio-temporal data (see, e.g., Reference [23] and the references therein). Kriging does not work on generic manifolds. For this reason, to perform the comparison with the new fixed point-based procedure, we combine kriging with a conformal flattening map approach, as detailed below.

Figure 3 shows the two test domains we considered for comparison purposes. The first domain is a benchmark geometry, employed, for instance, in Reference [12], here discretized by a mesh with 340 vertices. The second domain coincides with the geometry of a vessel, obtained after simplifying the patient-specific morphology of an inner carotid artery affected by an aneurysm, shown in the left panel of Figure 9.[24] This geometry is of relevance for the investigation carried out in Section 6.1. The mesh in the right panel of Figure 3, which discretizes the vessel geometry, is characterized by 600 vertices.

To generate data, over each manifold we consider 50 smooth functions defined by

$$f(\mathbf{p},t)=a_1\cos\left(2\pi p_{[1]}\left(1+\frac{t}{0.2}\right)\right)+a_2\cos\left(2\pi p_{[2]}\frac{t}{0.2}\right)+a_3\cos\left(2\pi p_{[3]}\right)\cos\left(2\pi\frac{t}{0.2}\right), \tag{14}$$

with $\mathbf{p}=[p_{[1]},p_{[2]},p_{[3]}]^T$, and where the coefficients $a_j$, for $j=1,2,3$, are randomly generated from independent normal distributions, with mean equal to zero and standard deviation equal to one. Then, these functions are evaluated at the mesh vertices (so that the data locations, $\mathbf{p}_1$, ..., $\mathbf{p}_n$, coincide with mesh vertices), in correspondence with 31 equispaced times in the time window [0, 0.3]. The collected values are hence corrupted by an additive independent Gaussian noise, with mean equal to zero and variance equal to 0.5. The noise level ranges approximately from 0% to 60% of the true signal.

The first column in Figures 4 and 5 shows the first smooth function generated according to (14) at different times, over Geometry 1 and 2, respectively. The second column in the same figures provides the corresponding sampled noisy data, at the same times.

Now, starting from the noisy data, we resort to the fixed point-based algorithm proposed in Section 4.2 to estimate the 50 smooth functions generated over the two benchmark geometries. To this aim, for both the test domains and for each simulation repetition, we select the smoothing parameter $\lambda$ in (2) via 5-fold cross validation,[25] while constraining the fixed point iterations with parameters `TOL` $=$ 5e$-$04 and `NMax` $=30$. The fixed point algorithm converges, on average, after 5 and 6 iterations for Geometry 1 and 2, respectively. The third columns in Figures 4 and 5 show the corresponding estimation, at the different times. The matching with the original data is very good, despite the noise characterizing the sampled data.

For the sake of comparison, we compute now the estimates by kriging.

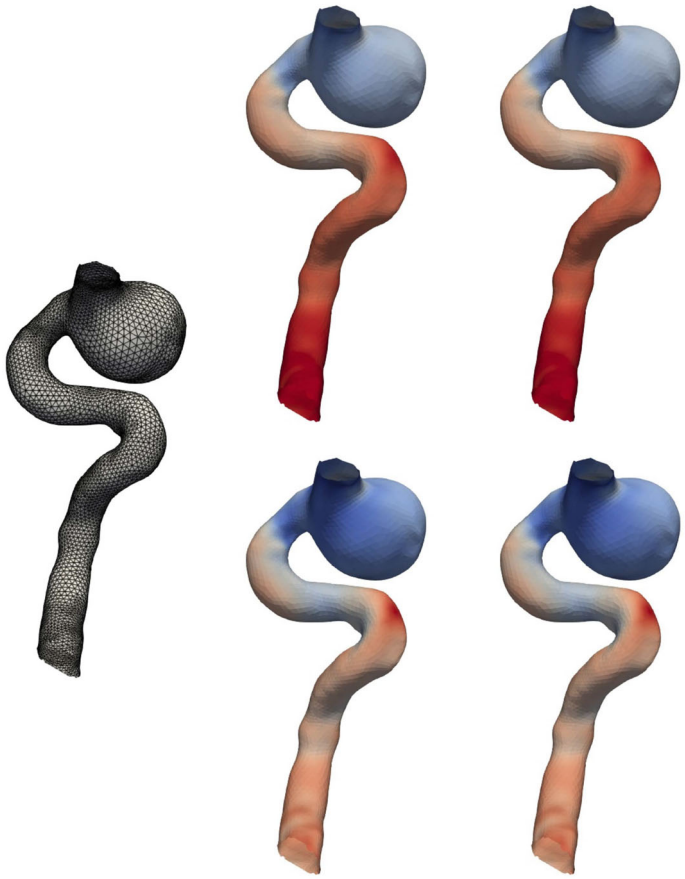

**FIGURE 9** Heamodynamic case study: discretization of the inner carotid artery (left); observed wall shear-stress (middle) and corresponding estimate provided by the fixed point-based approach (right) at two different temporal instants (top-bottom) during the heart beat

The bi-dimensional spatial domains kriging is able to handle are planar or spherical. This is not the case of Geometries 1 and 2. As a consequence, to implement kriging, we resort to a conformal flattening procedure according to what described in Reference [26]. In more detail, following Reference [12], we introduce a continuously differentiable map which changes the Riemannian manifold $\mathcal{M} \subset \mathbb{R}^3$ into a planar domain $\Omega \subset \mathbb{R}^2$. As an example, Figure 6 shows the result of the conformal flattening when applied to Geometry 1. Note that kriging does not employ the flattened mesh. This simply provides the location of the data on the conformally flattened domain, the data being located at the vertices of the planar mesh. Kriging is thus implemented over the flattened Geometries 1 and 2, by using the R package *gStat*.[27] In particular, we consider a separable variogram, marginally exponential in space and Gaussian in time, whose parameters, for each simulation replicate, are estimated starting from the values of the empirical variogram, as it is a standard practice for kriging.

Moreover, spatio-temporal kriging cannot handle too large datasets. This justifies the simplification we have applied to the original geometry of the patient-specific inner carotid artery (with an associated original mesh of 6017 vertices) to yield the mesh in Figure 3, right panel, consisting of 600 vertices only. The mesh simplification has been performed by exploiting the algorithm in Reference [10]. The fourth columns in Figures 4 and 5 provide the spatio-temporal kriging estimates at the considered times. A qualitative cross comparison among the third and the fourth columns in the two figures highlights the superior performances of the new algorithm proposed in Section 4.2. Indeed, for both the geometries, the fixed point-based algorithm succeeds in removing the artifacts introduced by the noise, while kriging turns out to be less effective on this respect.

We enrich the comparative analysis between the fixed point-based procedure and kriging by including the monolithic method adopted in Reference [17] and summarized in Section 4.1. The monolithic approach yields estimates which, from a qualitative viewpoint, are fully comparable with the results provided by the fixed point-based algorithm. Nevertheless, a quantitative investigation highlights that the method proposed in this paper outperforms the monolithic

formulation in terms of computational efficiency. The quantitative analysis is carried out by computing, for each test domain and for each simulation repetition, the Mean Square Error,

$$\mathrm{MSE} = \frac{\sum_{i=1}^{n}\sum_{j=1}^{m}\left[f(\mathbf{p}_i, t_j) - \widehat{f}(\mathbf{p}_i, t_j)\right]^2}{nm},$$

associated with the corresponding estimate, $\widehat{f}$, and the CPU time required by the computational procedure. Figure 7 collects the box plots for the MSE characterizing the three methods here compared, and for both the geometries. The performance of the fixed point-based algorithm and of the monolithic approach in terms of MSE is essentially the same. Instead, kriging exhibits a significantly higher MSE, with a large dispersion and several outliers associated with very high MSE values. As expected, the estimates yielded by the new and by the monolithic algorithms turn out to be more robust, as highlighted by the contained dispersion of the related MSEs.

Figure 8 displays the box plots for the execution time, measured in seconds ([s]), demanded by the fixed point-based and by the monolithic methods, when run on the two test geometries. This check reveals the evident superiority of the new algorithm with respect to the monolithic approach in terms of numerical efficiency, with a reduction of the execution time, on average, of about five times for both the geometries. Kriging has not been included in the figure, due to the remarkably higher time characterizing such a method (around 4 min for both the geometries instead of few seconds).

## 6 | CASE STUDIES

We here illustrate the effectiveness of the fixed point-based method through two applied case studies, after having verified the reliability and the computational efficiency of such an approach in the previous section.

The first case study concerns the analysis of the shear-stress exerted by the blood-flow over the wall of an inner carotid artery (see Section 6.1). The second application comes from the neurosciences and deals with the study of the neuronal activity on the cerebral cortex (see Section 6.2). Standard kriging cannot be used in these real-word applications (not even disregarding the complex geometry of the domains), due to the high dimensionality of the data.

### 6.1 | Study of heamodynamic forces on the arterial walls

As a first practical case study, we consider a medical disease whose incidence in the population is very high (around 10 cases per 100,000 people, with mortality or serious health conditions in 60% of cases[28]). We are referring to the rupture of a cerebral aneurysm, namely, of a large bulge that may modify the standard shape of a vessel wall in the brain. These deformations are very common in the adult population. In the vast majority of cases, cerebral aneurysms are totally asymptomatic and innocuous. The rupture of an aneurysm is an infrequent event, but unfortunately characterized by a very high mortality.

The origin of this pathology is still largely unknown. The study of the factors causing the development and the possible rupture of aneurysms has attracted lot of interest in the scientific and medical community (see, e.g., References [29,30]). It is believed that one of the main features influencing the aneurysm pathogenesis is the shear-stress exerted by the blood flow on the arterial wall. In particular, a strong variation of the shear-stress in space, and over the time of the heart-beat, is conjectured to be associated with the aneurysms formation, development and possible rupture; moreover, very low values of shear-stress are thought to be very dangerous (see Reference [30] and references therein). This haemodynamic stress is in turn dependent on the complex morphology of the vessel. For this reason, the study of the spatio-temporal behavior of the shear-stress in patient-specific geometries of arteries affected by cerebral aneurysms, is of great interest for advancing the knowledge on this pathology.

Figure 9 shows the considered medical configuration. It coincides with a patient-specific inner carotid artery affected by a large aneurysm. In particular, the wall of the artery has been discretized by a triangular mesh consisting of 6017 vertices (see Figure 9, left). Actually, we are dealing with the same manifold as in Section 5 (Geometry 2). However, the computational efficiency of the fixed point-based algorithm allows us to involve here a finer discretization of such a geometry, with a consequent higher reliability of the associated analysis. Concerning the analyzed data, we refer

to the AneuRisk project.[24] In particular, we consider the modulus of the wall shear-stress obtained from computational fluid dynamics simulations.[31,32] This quantity is available at the mesh vertices, at 100 temporal instants, that cover a full heart-beat. A first analysis of these data has been carried out in Reference [12], although restricted to a single time-instant.

Now, we exploit the fixed point-based approach to estimate the spatial wall shear-stress distribution over the inner carotid artery at two distinct times during the heart beat. For this purpose, we choose the smoothing parameter $\lambda$ by 5-fold cross validation, while selecting values 1e−04 and 50 for parameters `TOL` and `NMax`, respectively. Six fixed point iterations are demanded, on average, to ensure the convergence at each time, leading to a total elapsed time equal to 16.28 s. Figure 9 compares the raw (middle panels) with the estimated (right panels) wall shear-stress. A visual inspection does not highlight differences between the observed and the smoothed data. This is due to the fact that these data, obtained by computational fluid dynamics simulations, are characterized by very low noise, that is, order of magnitude lower than the data values. For this reason, the proposed algorithm, that correctly identifies the very high signal-to-noise ratio in the data, only filters out the high-frequency variation in the observations. Of course, a higher value of the smoothing parameter $\lambda$ could be used to return a smoother estimate, that highlights only the main patterns of the signal. The displayed temporal instants are characterized by a significative variation in the shear-stress distribution, in particular with low values of the shear stress within the aneurysmal sac. Independently of the selected time instants, it can be checked that in this location the wall shear-stress remains always very low and fluctuating, thus supporting the conjecture that low values of this stress play a major role in the aneurysmal pathogenesis.

## 6.2 | Study of neuronal activity on the cerebral cortex

The cerebral cortex is the outermost part of the brain - a thin layer of neural tissue where most of the neuronal activity takes place. From a geometric viewpoint, the cerebral cortex coincides with a highly tangled surface. It can be approximated by a triangular mesh which, unavoidably, turns out to be very complex, as shown in left panel of Figure 1. On the top of this two-dimensional manifold domain, it can be observed a time-varying hemodynamic signal associated with the neuronal activity on the cerebral cortex. Figure 1 shows one temporal snapshot of such a hemodynamic signal, measured during a functional Magnetic Resonance Imaging (fMRI) scan. The propagation of this signal constitutes the object of our investigation.

The data here analyzed come from the Human Connectome Project, a wide public database of resting-state and task-based fMRI scans, structural scans, diffusion MRI scans, from a large number of volunteers.[33] Currently, there is a strong effort in the scientific community in setting up methods for the analysis of this kind of data (see, e.g., References [8,34,35]), with the common goal of advancing the knowledge on cerebral functioning and diseases. Despite this considerable interest, the most part of neuroimaging studies is still carried out either by disregarding the spatial dependence

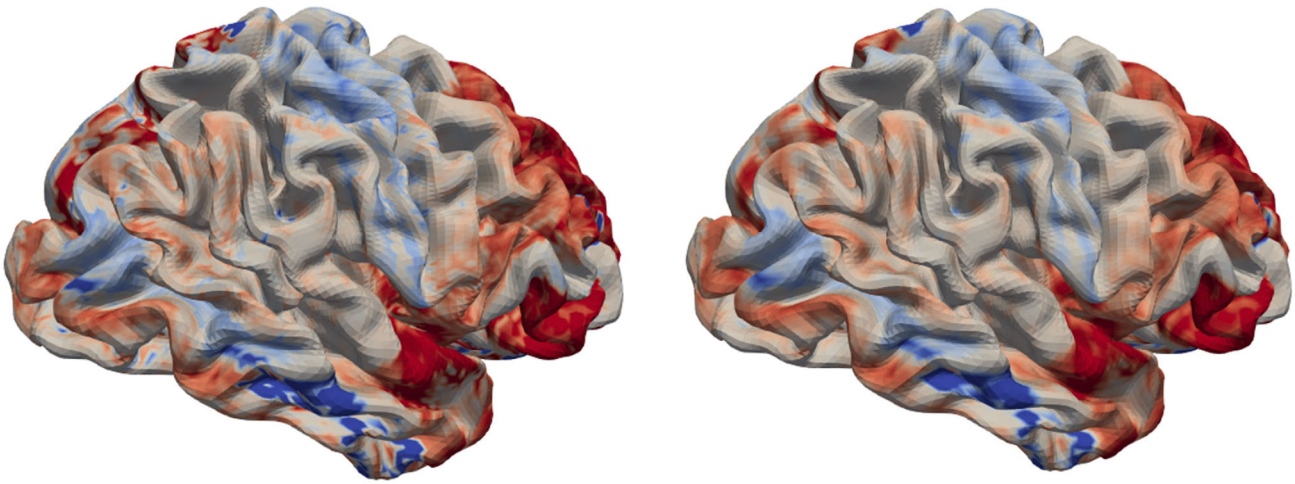

**FIGURE 10** Neuroimaging case study: observed signal at a fixed temporal instant (left) and corresponding estimate provided by the fixed point-based approach (right)

in the signal, or by employing basic methods which exploit the standard Euclidean distance. These simplified endeavors may lead to inaccurate estimates, for instance since functional distinct areas, that are apart over the cortex, result close in three-dimensional space due to the presence of a sulcus. Actually, it has been proved that the possibility to include the highly complex brain anatomy in the data analysis turns out to be a necessary step in order to guarantee a reliable investigation.[14,36] The method adopted in this paper offers a spatio-temporal smoothing procedure able to correctly comply with the cerebral cortex morphology.

To assess the fixed point-based algorithm, we start from the data associated with the triangular mesh in the left panel of Figure 1, consisting of 32,492 vertices. The data coincide with the fMRI signals induced over a patient-specific cerebral cortex by the neuronal activity, at 30 temporal instants. The left panel in Figure 10 shows a specific temporal snapshot of this signal. Starting from these noisy data, we run the algorithm proposed in Section 4.2 to estimate the underlying smooth spatio-temporal signal on the cerebral cortex. To this aim, we select the smoothing parameter in (2) by 5-fold cross validation and we set the two parameters, `NMax` and `TOL`, characterizing the stopping check to 50 and 1e−04, respectively. The fixed point algorithm converges, on average, within 15 iterations, while the whole estimation process takes 400.16 s. Figure 10, compares the raw data (left panel) with the smooth estimate provided by fixed point algorithm (right panel), at the considered temporal instant. A visual comparison between the two panels highlights the accuracy of the estimate, that is able to efficiently smooth the data, appropriately filtering out the noise without generating any artifact. In particular, notice that the data values observed over nearby gyri are not artificially linked by the algorithm.

Finally, we remark that higher values for parameter $\lambda$ could also be used in order to yield an estimate that only captures the macroscopic features of the original signal, thus returning the corresponding main pattern.

## 7 | DISCUSSION AND POSSIBLE ENHANCEMENTS

The proposed fixed point-based approach turns out to be an ideal tool to analyze large amount of spatio-temporal data over general manifolds in $\mathbb{R}^3$. The numerical assessment in Section 5 shows the superiority of such a new method when compared both with kriging (combined with a conformal flattening of the domain to manage generic manifolds) and with the monolithic procedure proposed in Reference [17], here adapted to non-planar domains. In particular, the fixed point-based algorithm is considerably more reliable than kriging (Figures 4, 5, 7). On the other hand, when compared with the monolithic approach, the new method reveals to be significantly more efficient in terms of computational time (Figure 8) without waiving the estimate accuracy (Figure 7), and allows us to handle data over general two-dimensional Riemannian manifolds. The gained effectiveness guarantees the possibility to estimate massive datasets as corroborated by the applicative settings analyzed in Section 6.

The method introduced in this paper enables several extensions. Among the most interesting ones, we cite the inclusion of space-varying covariates in a semi-parametric setting, analogously to what discussed in References [12,37] for the simplified case of spatial data only. In the heamodynamic framework, this feature would allow us to include into the estimation process the space-varying radius and the curvature of the vessel, to study the role played by these geometrical features in cerebral aneurysm pathology. In the application to neuroimaging data, we would take into account the space-varying cortical thickness, which may have an effect on the hemodynamic signal here considered.

Another interesting generalization concerns the adopted finite element discretization which could be replaced by an isogeometric analysis, thus generalizing what done in Reference [15] in a steady setting.

### ACKNOWLEDGMENTS

We are grateful to Eardi Lila for helping us in the processing of the brain imaging data. We also thank Bree Ettinger, who provided us the code implementing the conformal flattening used in Section 5, for comparison purposes with kriging. Finally, the second author acknowledges the research project GNCS-INdAM 2020 "Tecniche Numeriche Avanzate per Applicazioni Industriali." Open Access Funding provided by Politecnico di Milano within the CRUI-CARE Agreement.

### DATA AVAILABILITY STATEMENT

Research data are not shared.

## ORCID

*Simona Perotto* https://orcid.org/0000-0003-2994-7516

## ENDNOTE

* The computations of the paper have been run on a Asus Intel Core i7-7700HQ 2.80GHZ 16GB desktop computer.

## REFERENCES

1. Baramidze V, Lai MJ, Shum CK. Spherical splines for data interpolation and fitting. *SIAM J Sci Comput*. 2006;28(1):241-259.
2. Castruccio S, Stein ML. Global space-time models for climate ensembles. *Ann Appl Stat*. 2013;7(3):1593-1611.
3. Jeong J, Jun M. A class of Matérn-like covariance functions for smooth processes on a sphere. *Spat Stat*. 2015;11:1-18.
4. Lai MJ, Shum CK, Baramidze V, Wenston P. Triangulated spherical splines for geopotential reconstruction. *J Geodesy*. 2009;83(4):695-708.
5. Porcu E, Alegria A, Furrer R. Modelling temporally evolving and spatially globally dependent data. *Int Stat Rev*. 2018;86(2):344-377.
6. Porcu E, Bevilacqua M, Genton MG. Spatio-temporal covariance and cross-covariance functions of the great circle distance on a sphere. *J Am Stat Assoc*. 2016;111(514):888-898.
7. Wahba G. Spline interpolation and smoothing on the sphere. *SIAM J Sci Statist Comput*. 1981;2(1):5-16.
8. Chung M, Hanson J, Pollak S. Statistical analysis on brain surfaces. *Chapman & Hall/CRC Handbooks of Modern Statistical Methods*. CRC Press; 2017:233-262.
9. Chung MK, Robbins SM, Dalton KM, Davidson RJ, Alexander AL, Evans AC. Cortical thickness analysis in autism with heat kernel smoothing. *Neuroimage*. 2005;25:1256-1265.
10. Dassi F, Ettinger B, Perotto S, Sangalli LM. A mesh simplification strategy for a spatial regression analysis over the cortical surface of the brain. *Appl Numer Math*. 2015;90:111-131.
11. Duchamp T, Stuetzle W. Spline smoothing on surfaces. *J Comput Graph Stat*. 2003;12(2):354-381.
12. Ettinger B, Perotto S, Sangalli LM. Spatial regression models over two-dimensional manifolds. *Biometrika*. 2016;103(1):71-88.
13. Hagler DJ, Saygin AP, Sereno MI. Smoothing and cluster thresholding for cortical surface-based group analysis of fMRI data. *Neuroimage*. 2006;33:1093-1103.
14. Lila E, Aston JAD, Sangalli LM. Smooth principal component analysis over two-dimensional manifolds with an application to neuroimaging. *Ann Appl Stat*. 2016;10(4):1854-1879.
15. Wilhelm M, Dedè L, Sangalli LM, Wilhelm P. IGS: an IsoGeometric approach for smoothing on surfaces. *Comput Methods Appl Mech Eng*. 2016;302:70-89.
16. Sangalli LM. Spatial regression with partial differential equation regularization. *Int Stat Rev*. 2021;89:505-531.
17. Arnone E, Azzimonti L, Nobile F, Sangalli LM. Modeling spatially dependent functional data via regression with differential regularization. *J Multivariate Anal*. 2019;170:275-295.
18. Ern A, Guermond JL. *Theory and Practice of Finite Elements. 159 of Applied Mathematical Sciences*. Springer-Verlag; 2004.
19. Lila E, Sangalli LM, Ramsay J, Formaggia L. fdaPDE: functional data analysis and partial differential equations; statistical analysis of functional and spatial data, Based on Regression with Partial Differential Regularizations 2020. R package version 0.1-9.
20. Quarteroni A, Sacco R, Saleri F. *Matematica Numerica*. Springer-Verlag Italia; 1998.
21. Thomée V. *Galerkin Finite Element Methods for Parabolic Problems. 25 of Springer Series in Computational Mathematics*. Springer-Verlag; 2006.
22. Eriksson K, Estep D, Hansbo P, Johnson C. *Computational Differential Equations*. Cambridge University Press; 1996.
23. Cressie N, Wikle C. *Statistics for Spatio-Temporal Data*. Wiley; 2011.
24. AneuRisk project. https://statistics.mox.polimi.it/aneurisk/.
25. Hastie T, Tibshirani R, Friedman J. *The Elements of Statistical Learning*. 2nd ed. Springer Series in StatisticsSpringer; 2009 Data mining, inference, and prediction.
26. Halier S, Angenent S, Tannenbaurn A, Kikinis R. Nondistorting flattening maps and the 3-D visualization of colon CT images. *IEEE Trans Med Imaging*. 2000;19(7):665-670.
27. Pebesma E. Multivariable geostatistics in S: the gstat package. *Comput Geosci*. 2004;30:683-691.
28. Rinkel GJ, Djibuti M, Algra A, Van Gijn J. Prevalence and risk of rupture of intracranial aneurysms: a systematic review. *Stroke*. 1998;29(1):251-256.
29. Passerini T, Sangalli LM, Vantini S, et al. Integrated statistical investigation of internal carotid arteries of patients affected by cerebral aneurysms. *Cardiovasc Eng Technol*. 2012;3:26-40.
30. Bacigaluppi S, Piccinelli M, Antiga L, et al. Factors affecting formation and rupture of intracranial saccular aneurysms. *Neurosurg Rev*. 2014;37:1-14.
31. Passerini T. Computational hemodynamics of the cerebral circulation: multiscale modeling from the circle of Willis to cerebral aneurysms. *PhD Thesis Politecnico di Milano*. 2009.
32. Piccinelli M, Veneziani A, Steimann D, Remuzzi A, Antiga L. A framework for geometric analysis of 852 vascular structures: applications to cerebral aneurysms. *IEEE Trans Med Imaging*. 2009;28:1141-1155.

33. Essen DV, Ugurbil K, Auerbach E, et al. The human connectome project: a data acquisition perspective. *Neuroimage*. 2012;62(4):2222-2231.
34. Dassi F, Kroos J, Gerardo-Giorda L, Perotto S. A denoising tool for the reconstruction of cortical geometries from MRI. *Math Comput Simul*. 2022;191:14-32.
35. Worsley KJ, Liao CH, Aston J, et al. A general statistical analysis for fMRI data. *Neuroimage*. 2002;15(1):1-15.
36. Glasser MF, Sotiropoulos SN, Wilson JA, et al. The minimal preprocessing pipelines for the human connectome project. *Neuroimage*. 2013;80:105-124.
37. Sangalli LM, Ramsay JO, Ramsay TO. Spatial spline regression models. *J R Stat Soc Ser B Stat Methodol*. 2013;75(4):681-703.

**How to cite this article:** Ponti L, Perotto S, Sangalli LM. A PDE-regularized smoothing method for space–time data over manifolds with application to medical data. *Int J Numer Meth Biomed Engng*. 2022;38(12):e3650. doi:10.1002/cnm.3650